SCIENCE CHINA
Information Sciences

• RESEARCH PAPER •

April 2024, Vol. 67, Iss. 4, 142503:1–142503:8
https://doi.org/10.1007/s11432-023-3945-x

Quantum key distribution over a mimicked dynamic-scattering channel

Qi-Hang LU[1,2], Fang-Xiang WANG[1,2*], Wei CHEN[1,2,3*], Hai-Yang FU[1,2,3], Yin-Jie LU[1,2], Shuang WANG[1,2,3], De-Yong HE[1,2,3], Zhen-Qiang YIN[1,2,3], Guang-Can GUO[1,2] & Zheng-Fu HAN[1,2,3*]

[1]*CAS Key Laboratory of Quantum Information, University of Science and Technology of China, Hefei* 230026*, China;*
[2]*CAS Center for Excellence in Quantum Information and Quantum Physics, University of Science and Technology of China, Hefei* 230026*, China;*
[3]*Hefei National Laboratory, University of Science and Technology of China, Hefei* 230088*, China*

Received 26 September 2023/Revised 20 November 2023/Accepted 25 January 2024/Published online 27 March 2024

Abstract Free-space quantum key distribution (QKD) plays an important role in the global quantum network. However, free space channels suffer from the atmospheric turbulence and scattering effects of haze, fog, and dust, which significantly weaken the performance of QKD or even block the secure quantum link. Here, we prove the performance of QKD over a dynamic scattering channel can be enhanced significantly using a fast wavefront shaping technique. The system achieves on average 10-dB enhancement of quantum transmission efficiency and establishes a secure quantum link for QKD. Our work demonstrates the feasibility of QKD through free-space dynamic scattering channels and enhances the deployment capability of complex-channel QKD system.

Keywords quantum key distribution, free space channel, channel turbulence, channel scattering, wavefront shaping

1 Introduction

Quantum key distribution (QKD) [1–7] enables secure key distribution between distant users using fundamental principles of quantum mechanics. As an important part of the global quantum secure network, free-space QKD has been successfully deployed over ground-ground, ground-drone, and ground-satellite links. The transmission distances vary from 1 to 1000 km [8–16]. The free space channel easily suffers from turbulence and scattering effects [17–21]. Turbulence effects broaden, distort and deflect the transmitted beam [17,19–21]. The scattering particles (such as haze-and-fogs, clouds, and raindrops) can distort or even destruct the beam into speckles [18,22–27]. These effects weaken the system performance under diverse channel conditions and may even make it difficult to share secret keys [18–21,27], which hinders the deployment flexibility of free-space QKD.

The atmospheric turbulence effects can be mitigated by adaptive optics [11,14,28]. For strong scattering conditions, the beam is diffused into speckles and does not satisfy paraxial approximation. Thus, the more powerful wavefront shaping method becomes necessary [29]. The wavefront shaping method has been utilized to focus beam spot through scattering media [30,31] and to establish a secure QKD link over static strong scattering channel [32].

However, a practical free-space channel usually suffers from both turbulence and scattering effects simultaneously [18,33]. For example, the haze-and-fogs and clouds usually flow with turbulence and consist of a dynamic scattering channel. The dynamic scattering channel is strongly scattered with high loss and temporally variant (from sub-second to minutes [24,34]), and is difficult to predict or reproduce. These features lead to higher background noise, lower and unstable quantum transmission efficiency [35],

* Corresponding author (email: fxwung@ustc.edu.cn, weich@ustc.edu.cn, zfhan@ustc.edu.cn)

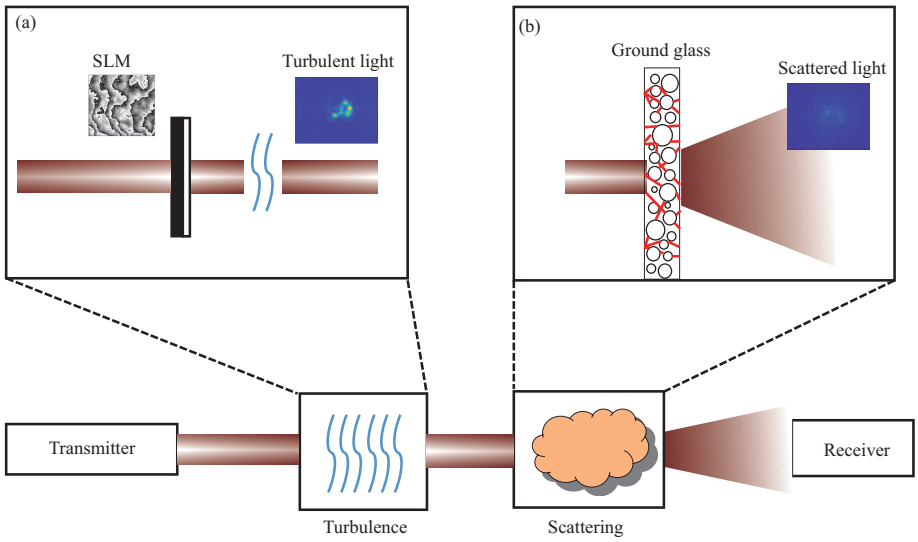

Figure 1 (Color online) Scheme of the emulated dynamic scattering channel. The dynamic scattering effects are considered the superimposing of the turbulence effects and the scattering effects. (a) The SLM with a turbulent phase screen and the propagation after it emulates the turbulence effects in the free space channel. (b) A piece of ground glass emulates the scattering effects. SLM: spatial light modulator.

and larger temporal jitters of photon arrival time [27], which weakens or even blocks the secure key distribution of free-space QKD.

To enhance the feasibility and performance of the free-space QKD system, it is required further study of the evolution mechanism of the dynamic scattering effects on photon states and the development of a fast optimization method to compensate for the adverse turbulent and scattering effects.

Researchers have utilized the theoretical simulation [18, 26, 27, 33, 36, 37] and laboratory emulation methods [34, 38, 39] to describe and simulate the dynamic scattering channel. The theoretical simulation models give a description of different types of dynamic scattering mechanisms in free space [18, 27, 33, 36], among which the Vasylyev model gives a quantifiable evaluation by decomposing the turbulence and scattering effects [18]. In the laboratory, such a channel is usually emulated by the atmospheric chamber [34,38,40]. It offers a convenient manner for measuring and analyzing the channel characteristics. However, the chamber is not repeatable and hard to quantify. It makes the precise evaluation of the dynamic channel effects hard to accomplish. Without a controllable dynamic scattering channel, it will be difficult to develop an effective wavefront shaping method to improve the transmission fidelity and efficiency of photon states over the dynamic complex channel, let alone establish a secure quantum link [41–43].

In this work, we establish a controllable and quantifiable dynamic scattering channel in the laboratory. Based on the emulated channel, we develop an effective fast wavefront shaping technique and achieve on average 10-dB enhancement of transmission efficiency within tens of seconds. Then, a secure quantum link is established, within which secure key distribution is successfully realized. This work can offer an effective way to improve the performance of the free-space QKD systems over complex channel conditions.

2 Mimicked dynamic-scattering channel

For free-space QKD, the index fluctuations of the channel induced by turbulence and scattering can be considered to be independent and the corresponding fluctuation spectrum becomes [18]

$$\Phi_\epsilon(\boldsymbol{\kappa}) = \Phi_\epsilon^{\mathrm{turb}}(\boldsymbol{\kappa}) + \Phi_\epsilon^{\mathrm{scatt}}(\boldsymbol{\kappa}), \tag{1}$$

where $\boldsymbol{\kappa}$ is proportional to the transverse wave vector, $\Phi_\epsilon^{\mathrm{turb}}(\boldsymbol{\kappa})$ is the turbulence-induced spectrum, and $\Phi_\epsilon^{\mathrm{scatt}}(\boldsymbol{\kappa})$ is the scatter-induced spectrum.

According to the above model, we build a dynamic scattering channel (as shown in Figure 1) by combining the time-variant turbulence (Figure 1(a)) with a static scattering medium (Figure 1(b)). The time-variant turbulence is emulated by displaying distorted phase screens on the spatial light modulator

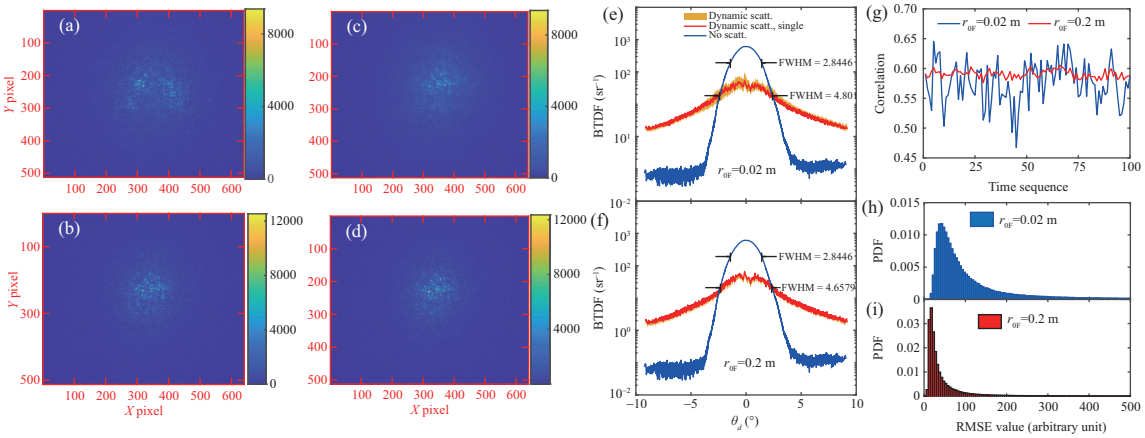

Figure 2 (Color online) (a–d) Spot images after passing through the dynamic scattering channel corresponding to coherence lengths $r_{0\mathrm{F}} = 0.02$ m ((a) and (b)), and $r_{0\mathrm{F}} = 0.2$ m ((c) and (d)), respectively. (a) and (c) are real-time spot images while (b) and (d) are average spot images. (e, f) The BTDF of the dynamic scattering channel corresponding to coherence lengths (e) $r_{0\mathrm{F}} = 0.02$ m and (f) $r_{0\mathrm{F}} = 0.2$ m, respectively. (g) The inner product of a series of dynamic scattered spots under different coherence lengths $r_{0\mathrm{F}}$ with the Gaussian spot. (h, i) The probability distribution functions of the root-mean-square errors of 100 dynamically scattered speckles under coherence lengths (h) $r_{0\mathrm{F}} = 0.02$ m and (i) $r_{0\mathrm{F}} = 0.2$ m. All the screens above have a wind speed $N_{\mathrm{sF}} = 0.5$ m/s. Color bars: Pixel value. Camera exposure time: 16.7 ms in (a)–(d), (h) and 80 ms in (e)–(g). Pixel pitch on camera: 20 μm. No scatt.: No scattering. Dynamic scatt.: Dynamic scattering.

(SLM) [44] (details shown in Appendix A), according to the Taylor frozen hypothesis [45]. The scattering effect is realized by the ground glass inserted after the SLM. Since the beam after the turbulence modulator becomes distorted in space and the scattering effect is position sensitive, the beam that goes through the complex channel will evolve to different turbulent and scattering patterns at different times. Therefore, an effective dynamic scattering channel can be mimicked.

The dynamic scattering channel is determined by strengths of turbulence and scattering, and their corresponding spatial and temporal modes. The strength of turbulence effect on a specific optical system is characterized by the Fried parameter (also called coherence length) $r_0 = (0.423k^2C_n^2L)^{-3/5}$, where L is the channel length, $k = \frac{2\pi}{\lambda}$ is the optical wave number, and C_n^2 is the turbulence structure constant [46]. The scattering strength can be evaluated by the bidirectional transmission distribution function (BTDF) [47], which is the function of scattered direction angle θ_d of the beam

$$\mathrm{BTDF}(\theta_d) = \frac{\phi_s(\theta_d)}{\phi_i(\theta_d)\mathrm{d}\Omega\cos\theta_d}. \tag{2}$$

The details of BTDF are shown in Appendix B. The correlation between the scattered spot and Gaussian beam (no scattering), which is defined as Correlation $= \langle I_s I_i \rangle$ with I_s (I_i) the normalized intensity distribution of the (no) scattered beam, reflects the change of spatial mode. The spatial mode also varies with time and is correlated with the temporal evolution feature of the dynamic channel (turbulence and position-sensitive scattering).

We emulate the free-space dynamic scattering channel on the table as shown in Figure 1, which includes the SLM and the ground glass. The dynamic channel characteristic is emulated by adopting the shifted-phase-screen method [48,49] with a certain r_0. The shifting speed of the phase screen corresponds to wind speed N_{s}. The mapping function of the Fried parameter and wind speed between the in-table channel and a longer free-space field can be determined by the Fresnel scaling equation [44, 46]

$$r_{0\mathrm{F}} = A_{\mathrm{m}}r_0, N_{\mathrm{sF}} = A_{\mathrm{m}}N_{\mathrm{s}}, A_{\mathrm{m}} = \sqrt{\frac{L_{\mathrm{field}}}{L_{\mathrm{table}}}}, \tag{3}$$

where A_{m} is the scaling factor and L_{field} (L_{table}) is the channel length in the field (table). Our emulated dynamic scattering channel is 1.35 m and the diameter of the input Gaussian beam is 3 mm. We can then rescale the emulated channel to a 540 m field channel with a scaling factor $A_{\mathrm{m}} = 20$ (see Appendix A for more discussion). The emulated channel is easily reproducible by replaying the turbulence phase screens. Hence, we could give precise temporal and statistical features of the dynamic scattering channel.

Figures 2(a) and (b) and 2(c) and (d) give the instantaneous and average spatial intensity distributions of light beam through the dynamic scattering channel with $r_{0\mathrm{F}} = 0.02$ m and 0.2 m, respectively. The

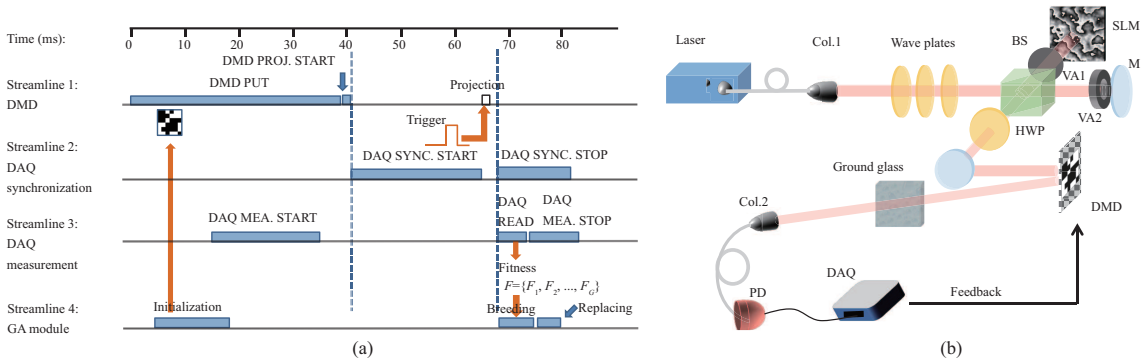

Figure 3 (Color online) (a) Time-flowchart of the DMD-based fast compensation system. (b) Experimental setup for the static and dynamic scattering channel optimization system. BS: beam splitter; VA: variable aperture; M: mirror; SLM: spatial light modulator; HWP: half wave plate; DMD: digital-micromirror-devices; Col.1 and Col.2: fiber collimators; PD: photoelectric detector; DAQ: data acquisition system. DMD PROJ.START: DMD projection start; DAQ MEA. START: DAQ measurement start; DAQ SYNC. START: DAQ synchronization start; DAQ SYNC. STOP: DAQ synchronization stop; DAQ MEA. STOP: DAQ measurement stop.

incident Gaussian beams are strongly scattered into speckles and the spatial distribution range is wider for stronger turbulence ($r_{0\mathrm{F}} = 0.02$). The full width at half maximum (FWHM) of BTDF (Figure 2(e)) of the beam through the dynamic channel with $r_{0\mathrm{F}} = 0.02$ m is expanded by 1.7 times (from 2.85 to 4.80 degree). The FWHM and fluctuation decrease with turbulence strength, according to the red lines and yellow background in Figures 2(e) and (f). The correlations between the scattered speckles and Gaussian beam are given in Figure 2(g). As turbulence becomes stronger, the correlation is lower and the temporal fluctuation is larger. We then evaluate the fluctuation of speckles through the emulated channel. We calculate the root-mean-square errors (RMSEs) of 100 speckle beams and give probability distribution functions (PDF) in Figures 2(h) and (i). The PDF is much fatter for smaller $r_{0\mathrm{F}}$ and it indicates a stronger dynamic channel.

The results demonstrate that the dynamic scattering channel seriously distorts the spatial mode of the beam and the scattered intensity distribution varies with time. The dynamic channel effects will deteriorate the receiving efficiency and increase the corresponding variance significantly, which weakens the performance of QKD.

3 Rapid feedback optimization system

To mitigate the dynamic scattering effects of the complex channel, a rapid feedback module is necessary. On the other hand, an anti-noise optimization algorithm will make the feedback efficient and stable. The genetic algorithm (GA) is known for its global search and anti-noise abilities and has been successfully applied in wavefront shaping [31] and in mitigating the static scattering effect of QKD [32]. The characteristic varying time of the dynamic scattering is from 1 s to 1 min [24, 34]. Therefore, the optimization should be effectively fulfilled within one minute.

Here in Figure 3, we combine the fast binary-amplitude-modulated digital-micromirror-devices (DMD, 10-kHz modulation frequency) with the GA to realize a rapid wavefront shaping module through the dynamic scattering channel, so that the feedback optimization system could decrease the channel loss significantly (Appendix C shows more details of the GA procedure). The wavefront modulation patterns of every generation are loaded on the DMD with a speed of 100 μs per pattern (20 patterns per generation). The intensity through the channel is measured by a PD and a data acquisition (DAQ) card. To establish a QKD link through the dynamic scattering channel, improving the channel transmission efficiency is important. Thus, the fitness function of GA, which determines the breeding parents for the offspring, is defined as the channel efficiency.

We have designed a 4-parallel-work-line feedback procedure to achieve efficient optimization (Figure 3(a)). The whole process consists of 3 stages. In the first stage (preparation), the DMD receives the binary modulation patterns (DMD PUT, 39 ms), prepares for projection and waits for the synchronization signal (DMD PROJ. START, 2 ms). Parallelly, the DAQ card prepares for signal measurement (DAQ MEA. START) and the GA module prepares for breeding. In the second stage, the DAQ card outputs the synchronization signal (22 ms) and the DMD performs the projection process (2 ms) subsequently. In the third stage, the DAQ card reads (DAQ READ), transfers the photodetector signal to the GA module

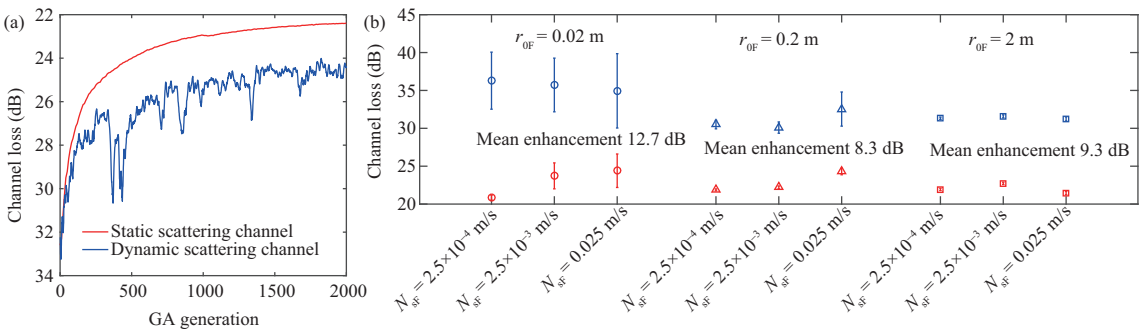

Figure 4 (Color online) Optimization results. (a) The change of the channel loss in dB during the optimization process of the static (red line) and dynamic (r_{0F} = 0.2 m, N_{sF} = 0.025 m/s, blue line) strong scattering channel. (b) The channel losses before (blue data with error bar) and after optimization (red data with error bar) of dynamic scattering channels under different turbulence parameters r_{0F} and N_{sF}. The circles, triangles, and squares correspond to r_{0F} = 0.02 m, 0.2 m, and 2 m, respectively. All optimizations are implemented for 2000 generations from the same initial population.

(5 ms), and stops the measurement procedure (DAQ MEA. STOP, 7 ms). The GA module costs 8 ms (including breeding and replacing processes, see Appendix C for more details) for every generation. At the same time, the DAQ card stops the synchronization (DAQ SYNC. STOP) procedure (14 ms). With careful design, the total time cost of one feedback loop is about 80 ms. A real-time optimization of the dynamic scattering channel can then be fulfilled within tens of seconds (hundreds of iterations).

The optical setup of the optimization system is shown in Figure 3(b) (more details are shown in Appendix D). A laser beam with a 1550 nm wavelength and beam width of 3 mm is collimated into free space. Then the beam passes through a beam splitter (BS) and is split into two paths, which are controlled by two variable apertures (VA1 and VA2). The reflective path passes through the SLM and the scattering medium to emulate the dynamic scattering channel, while the transmission path emulates the static scattering channel only. The strong scattering medium is realized by inserting a ground glass in the channel. No matter which path it passes through, the beam will be projected onto the DMD for amplitude modulation. After transmitting through the channel, by considering the sensitivity of the QKD system to signal-to-noise ratio (SNR), we choose the single mode fiber (SMF) to collect the photons so as to suppress the background noise from free space channel [12, 50]. The photon signal is then detected by a photodetector (PD) and a DAQ card.

To verify the effectiveness of the fast optimization procedure, we first implement it through a static scattering channel. In this scenario, the SLM is blocked by an aperture. We run the GA optimization for 2000 iterations and achieve 10.2-dB enhancement of transmission efficiency (the red line in Figure 4(a)). The optimization enhancement approaches 10 dB with a time cost of 40 s (500 iterations).

We then verify the real-time performance of the feedback system over the dynamic scattering channel, where the path through the SLM is open and the mirror path is blocked. The optimization is run by 2000 generations under different dynamic scattering channel conditions. The optimization enhancement under $r_{0F} = 0.2$ m ($C_n^2 \simeq 4.57 \times 10^{-15}$ m$^{-2/3}$, moderate turbulence) and $N_{sF} = 0.025$ m/s (calm wind) is shown as the blue line in Figure 4(a). An enhancement of 8.2 dB is achieved. Compared with the static scattering channel, there exists random time-variant fluctuation caused by the dynamic evolution feature of the channel, as shown in Figure 2. Nevertheless, the optimization still achieves significant enhancement since the fluctuation is slow compared with the feedback speed. The average optimization enhancements under different coherence lengths r_{0F} and wind speeds N_{sF} are 10.1 dB (Figure 4(b)). Benefitting from the fast wavefront shaping technique, the system achieves a significant optimization enhancement under dynamic scattering conditions. When the wind speed is fixed, the enhancement fluctuation increases with stronger turbulence. For example, when $N_{sF} = 2.5 \times 10^{-3}$ m/s, the optimization enhancement fluctuation under weak ($r_{0F} = 2$ m) turbulent strength is 1 order smaller than that under strong ($r_{0F} = 0.02$ m) turbulence strength. The performance of the feedback system also depends on the wind speed. For example, under $r_{0F} = 0.2$ m, when the wind speed increases from $N_{sF} = 2.5 \times 10^{-3}$ m/s to $N_{sF} = 0.025$ m/s, the optimization fluctuation increases almost 3 times.

Increasing the system optimization speed is equivalent to decreasing the wind speed N_s. By integrating the feedback process into the field programmable gate array (FPGA) hardware, the DMD can reach a frame rate of 10 kHz (40 times faster than our current system) and the time consumption of the software tache per iteration round will be negligible. Thus, the total time consumption of the optimization will only

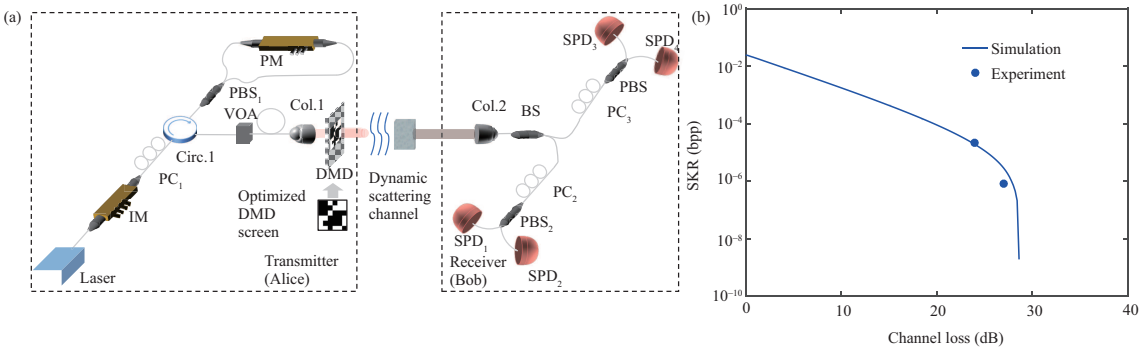

Figure 5 (Color online) (a) Setup of the QKD system. VOA: variable optical attenuator; BS: beam splitter; DMD: digital-micromirror-devices; Col.1 and Col.2: fiber collimators; IM: intensity modulator; PBS: polarized beam splitter; PC: polarization controller; Circ.: circulator; PM: phase modulator; SPD: single photon detector. (b) Secure key rates of the QKD experiment under the channel condition of $r_{0\mathrm{F}} = 0.02$ m and $N_{\mathrm{sF}} = 0.025$ m/s. The blue line and dots are the simulation and experimental key rates under the block length of $N = 10^9$, respectively.

be determined by the speeds of wavefront manipulation and convergence of the algorithm. By updating the feedback system with an FPGA-based genetic algorithm or the machine learning algorithms [51–53], the speed wavefront shaping system using DMD can be increased by 1–2 orders. Considering the state-of-the-art technologies, the wavefront manipulation time cost is hopefully to be reduced to μs [54, 55] and the optimization speed is perspective to be enhanced further. With the improvements above, the optimization can be achieved at the extreme condition of $N_{\mathrm{sF}} = 100$ m/s (violent storm) at $r_{0\mathrm{F}} = 0.02$ m (strong turbulence).

4 Establishing a secure quantum key distribution (QKD) link

After optimization, we implement a proof-of-principle polarization-based BB84 QKD experiment over the dynamic scattering channel. The Z and X bases are $\{|H\rangle, |V\rangle\}$ and $\{|+\rangle, |-\rangle\}$, respectively. These states correspond to horizontal, vertical, 45° and 135° linear polarization, separately. The setup of the QKD system is shown in Figure 5(a). At the transmitter's (Alice's) side, the photon states are prepared by the fiber-based Sagnac interferometer [56], where a phase modulator (PM) is inserted asymmetrically into the Sagnac loop. The polarization controller (PC_1) before the Sagnac loop is to maintain the input polarization state as $|+\rangle$. A distributed feedback (DFB) pulsed laser (1550 nm, beam diameter 3 mm, repetition rate (system frequency) 10 MHz) is used as the light source. The intensity modulator (IM) is to prepare decoy states. As a proof-of-principle experiment, the photon states are not randomly prepared. A variable optical attenuator (VOA) attenuates the pulses to a single-photon level. For the receiver (Bob), a beam splitter (BS) is used to passively choose the measurement basis. In each path, a polarized beam splitter (PBS_2 and PBS_3) and two single photon detectors (SPD_1–SPD_4) are used to implement the projection measurement of Z or X bases. The PCs (PC_2 and PC_3) in the receiver compensate for the slow drifts of polarization. The average detection efficiency and the dark count rate of the SPDs are 23.5% and 1.09×10^{-6}/gate, respectively. The Alice's side and Bob's side are synchronized by electrical methods.

By adopting two-intensity decoy-state method [57–59] and considering finite-key effect [60, 61], the secure key length can be extracted by

$$l = s_{z,0} + s_{z,1} - s_{z,1} H_2(\phi_z) - \lambda_{\mathrm{EC}} - 6\log_2\left(\frac{21}{\epsilon_{\mathrm{sec}}}\right) - \log_2\left(\frac{2}{\epsilon_{\mathrm{cor}}}\right), \tag{4}$$

where $s_{z,0}$ is the number of vacuum events, $s_{z,1}$ is the number, and ϕ_z is the phase error rate (upper bound) of single photon events in the Z basis, respectively; ϵ_{sec} and ϵ_{cor} are the security parameters of correctness and secrecy, respectively; the parameter λ_{EC} is the size of the information exchanged during the error-correction step, which is set as $n_z f_{\mathrm{EC}} h(e_{\mathrm{obs}})$, where e_{obs} is the average of the observed error rates in basis Z. According to (4), the secure key rate can be defined as $R = l/N$, where N is the block length.

The simulation and experimental finite-length secure key rates with a block length $N = 1 \times 10^9$ are shown in Figure 5(b). The average channel loss before optimization under different dynamic scattering

strengths is all beyond 30 dB, while that after optimization is less than 25 dB. That means we are finally able to build up a secure QKD link through the dynamic scattering channel. The experimental data demonstrates that a secure key rate of 2.20×10^{-5} bit per pulse has been achieved under the moderate dynamic scattering condition ($r_{0\mathrm{F}} = 0.2$ m and $N_{\mathrm{sF}} = 0.025$ m/s). While there is no secure key rate before optimization (channel loss is 32.4 dB). The experimental data also shows that the system can tolerate an extra channel loss of over 3 dB to ensure the continuous running of the QKD system.

5 Summary

In summary, we have emulated a free-space dynamic scattering channel, implemented a rapid feedback module to improve the transmission efficiency and established a secure quantum link for QKD. The dynamic scattering channel is adjustable and reproducible, so that precise evaluation can be fulfilled. The enhancement achieved by the rapid feedback module is on average 10 dB and the secure quantum link is established within tens of seconds. The system is promising for realizing secure key distribution under extreme channel conditions with further improvement. Our work enhances the deployment flexibility of practical free-space QKD systems over complex channels.

Acknowledgements This work was supported by National Natural Science Foundation of China (Grant Nos. 62371437, 62271463, 62171424), Fundamental Research Funds for the Central Universities (Grant No. KY2470000006), Innovation Program for Quantum Science and Technology (Grant No. 2021ZD0300701), and Plan for Major Anhui Provincial Science & Technology Project (Grant No. 202103a13010002).

Supporting information Appendixes A–D. The supporting information is available online at info.scichina.com and link.springer.com. The supporting materials are published as submitted, without typesetting or editing. The responsibility for scientific accuracy and content remains entirely with the authors.

References

1 Bennett C H, Brassard G. Quantum cryptography: public key distribution and coin tossing. In: Proceedings of the IEEE International Conference on Computers, Systems and Signal Processing, 1984
2 Xu F, Ma X, Zhang Q, et al. Secure quantum key distribution with realistic devices. Rev Mod Phys, 2020, 92: 025002
3 Fan-Yuan G-J, Chen W, Lu F Y, et al. A universal simulating framework for quantum key distribution systems. Sci China Inf Sci, 2020, 63: 180504
4 Zhang G-W, Chen W, Fan-Yuan G-J, et al. Polarization-insensitive quantum key distribution using planar lightwave circuit chips. Sci China Inf Sci, 2022, 65: 200506
5 Ren S, Wang Y, Su X L. Hybrid quantum key distribution network. Sci China Inf Sci, 2022, 65: 200502
6 Ma L, Yang J, Zhang T, et al. Practical continuous-variable quantum key distribution with feasible optimization parameters. Sci China Inf Sci, 2023, 66: 180507
7 Feng Y, Qiu R H, Zhang K, et al. Secret key rate of continuous-variable quantum key distribution with finite codeword length. Sci China Inf Sci, 2023, 66: 180511
8 Jacobs B C, Franson J D. Quantum cryptography in free space. Opt Lett, 1996, 21: 1854
9 Schmitt-Manderbach T, Weier H, Fürst M, et al. Experimental demonstration of free-space decoy-state quantum key distribution over 144 km. Phys Rev Lett, 2007, 98: 010504
10 Bedington R, Arrazola J M, Ling A. Progress in satellite quantum key distribution. npj Quantum Inf, 2017, 3: 30
11 Liao S K, Cai W Q, Liu W Y, et al. Satellite-to-ground quantum key distribution. Nature, 2017, 549: 43–47
12 Liao S K, Yong H L, Liu C, et al. Long-distance free-space quantum key distribution in daylight towards inter-satellite communication. Nat Photon, 2017, 11: 509–513
13 Yin J, Li Y H, Liao S K, et al. Entanglement-based secure quantum cryptography over 1,120 kilometres. Nature, 2020, 582: 501–505
14 Cao Y, Li Y H, Yang K X, et al. Long-distance free-space measurement-device-independent quantum key distribution. Phys Rev Lett, 2020, 125: 260503
15 Chen Y A, Zhang Q, Chen T Y, et al. An integrated space-to-ground quantum communication network over 4,600 kilometres. Nature, 2021, 589: 214–219
16 Moschandreou E, Rollick B J, Qi B, et al. Experimental decoy-state Bennett-Brassard 1984 quantum key distribution through a turbulent channel. Phys Rev A, 2021, 103: 032614
17 Vasylyev D, Semenov A, Vogel W. Atmospheric quantum channels with weak and strong turbulence. Phys Rev Lett, 2016, 117: 090501
18 Vasylyev D, Semenov A A, Vogel W, et al. Free-space quantum links under diverse weather conditions. Phys Rev A, 2017, 96: 043856
19 Liorni C, Kampermann H, Bruß D. Satellite-based links for quantum key distribution: beam effects and weather dependence. New J Phys, 2019, 21: 093055
20 Scriminich A, Foletto G, Picciariello F, et al. Optimal design and performance evaluation of free-space quantum key distribution systems. Quantum Sci Technol, 2022, 7: 045029
21 Pirandola S. Limits and security of free-space quantum communications. Phys Rev Res, 2021, 3: 013279
22 Liu C H, Yeh K C. Propagation of pulsed beam waves through turbulence, cloud, rain, or fog. J Opt Soc Am, 1977, 67: 1261
23 Deepak A, Farrukh U O, Zardecki A. Significance of higher-order multiple scattering for laser beam propagation through hazes, fogs, and clouds. Appl Opt, 1982, 21: 439
24 Muhammad S S. Characterization of fog attenuation in terrestrial free space optical links. Opt Eng, 2007, 46: 066001

25 Ijaz M, Ghassemlooy Z, Le Minh H, et al. Analysis of fog and smoke attenuation in a free space optical communication link under controlled laboratory conditions. In: Proceedings of International Workshop on Optical Wireless Communications (IWOW), 2012. 1–3
26 Mahalati R N, Kahn J M. Effect of fog on free-space optical links employing imaging receivers. Opt Express, 2012, 20: 1649–1661
27 Grabner M, Kvicera V. Multiple scattering in rain and fog on free-space optical links. J Lightwave Technol, 2014, 32: 513–520
28 Ge Y M, Wu L, Zhang C, et al. Orbital angular momentum multiplexing communication system over atmospheric turbulence with K-best detection. Sci China Inf Sci, 2021, 64: 192302
29 Vellekoop I M. Feedback-based wavefront shaping. Opt Express, 2015, 23: 12189–12206
30 Popoff S M, Lerosey G, Carminati R, et al. Measuring the transmission matrix in optics: an approach to the study and control of light propagation in disordered media. Phys Rev Lett, 2010, 104: 100601
31 Conkey D B, Brown A N, Caravaca-Aguirre A M, et al. Genetic algorithm optimization for focusing through turbid media in noisy environments. Opt Express, 2012, 20: 4840
32 Lu Q H, Wang F X, Huang K, et al. Quantum key distribution over a channel with scattering. Phys Rev Appl, 2022, 17: 034045
33 Yang R, Han J, Liang L, et al. Joint channel model for fog and atmospheric turbulence and performance analysis of unmanned aerial vehicles' free-space optical communication. Opt Eng, 2023, 62: 016104
34 Ijaz M, Ghassemlooy Z, Pesek J, et al. Modeling of fog and smoke attenuation in free space optical communications link under controlled laboratory conditions. J Lightwave Technol, 2013, 31: 1720–1726
35 Esmail M A, Fathallah H, Alouini M S. Outdoor FSO communications under fog: attenuation modeling and performance evaluation. IEEE Photonics J, 2016, 8: 1–22
36 Lukin I P, Rychkov D S, Falits A V, et al. A phase screen model for simulating numerically the propagation of a laser beam in rain. Quantum Electron, 2009, 39: 863–868
37 Yuan K, Wang Y H, Shen L F, et al. Sub-THz signals' propagation model in hypersonic plasma sheath under different atmospheric conditions. Sci China Inf Sci, 2017, 60: 113301
38 Khan A N, Saeed S, Naeem Y, et al. Atmospheric turbulence and fog attenuation effects in controlled environment FSO communication links. IEEE Photon Technol Lett, 2022, 34: 1341–1344
39 Liu Y, Yang X, Zhang H, et al. Quantitative scattering models of broad-band narrow-beam light through fog. Opt Express, 2022, 30: 35125–35135
40 Mao Z, Jaiswal A, Wang Z, et al. Single frame atmospheric turbulence mitigation: a benchmark study and a new physics-inspired transformer model. In: Proceedings of European Conference on Computer Vision, 2022. 430–446
41 Gong Y H, Yang K X, Yong H L, et al. Free-space quantum key distribution in urban daylight with the SPGD algorithm control of a deformable mirror. Opt Express, 2018, 26: 18897–18905
42 Jin J, Bourgoin J P, Tannous R, et al. Genuine time-bin-encoded quantum key distribution over a turbulent depolarizing free-space channel. Opt Express, 2019, 27: 37214–37223
43 Zhao J, Zhou Y, Braverman B, et al. Performance of real-time adaptive optics compensation in a turbulent channel with high-dimensional spatial-mode encoding. Opt Express, 2020, 28: 15376
44 Rodenburg B, Mirhosseini M, Malik M, et al. Simulating thick atmospheric turbulence in the lab with application to orbital angular momentum communication. New J Phys, 2014, 16: 033020
45 Taylor G I. The spectrum of turbulence. Proc R Soc Lond A, 1938, 164: 476–490
46 Li S, Chen S, Gao C, et al. Atmospheric turbulence compensation in orbital angular momentum communications: advances and perspectives. Optics Commun, 2018, 408: 68–81
47 Bartell F O, Dereniak E L, Wolfe W L, et al. The theory and measurement of bidirectional reflectance distribution function (Brdf) and bidirectional transmittance distribution function (BTDF). In: Proceedings of SPIE, 1981. 257: 154–160
48 Harding C M, Johnston R A, Lane R G. Fast simulation of a kolmogorov phase screen. Appl Opt, 1999, 38: 2161
49 Dios F, Recolons J, Rodríguez A, et al. Temporal analysis of laser beam propagation in the atmosphere using computer-generated long phase screens. Opt Express, 2008, 16: 2206
50 Gruneisen M T, Flanagan M B, Sickmiller B A. Modeling satellite-Earth quantum channel downlinks with adaptive-optics coupling to single-mode fibers. Opt Eng, 2017, 56: 126111
51 Sinha A, Lee J, Li S, et al. Lensless computational imaging through deep learning. Optica, 2017, 4: 1117
52 Liu J Y, Jiang Q Q, Ding H J, et al. Highly efficient twin-field quantum key distribution with neural networks. Sci China Inf Sci, 2023, 66: 189402
53 Bai B W, Shu H W, Wang X J, et al. Towards silicon photonic neural networks for artificial intelligence. Sci China Inf Sci, 2020, 63: 160403
54 Zhang X, Kwon K, Henriksson J, et al. A large-scale microelectromechanical-systems-based silicon photonics LiDAR. Nature, 2022, 603: 253–258
55 Zheng Z P, Huang Y J, Wu F, et al. Multidimensional modulation of light fields via a combination of two-dimensional materials and meta-structures. Sci China Inf Sci, 2023, 66: 160403
56 Li Y P, Chen W, Wang F X, et al. Experimental realization of a reference-frame-independent decoy BB84 quantum key distribution based on Sagnac interferometer. Opt Lett, 2019, 44: 4523
57 Wang X B. Beating the photon-number-splitting attack in practical quantum cryptography. Phys Rev Lett, 2005, 94: 230503
58 Lo H K, Ma X, Chen K. Decoy state quantum key distribution. Phys Rev Lett, 2005, 94: 230504
59 Ma X, Qi B, Zhao Y, et al. Practical decoy state for quantum key distribution. Phys Rev A, 2005, 72: 012326
60 Lim C C W, Curty M, Walenta N, et al. Concise security bounds for practical decoy-state quantum key distribution. Phys Rev A, 2014, 89: 022307
61 Lim C C W, Xu F, Pan J W, et al. Security analysis of quantum key distribution with small block length and its application to quantum space communications. Phys Rev Lett, 2021, 126: 100501